RSC Advances

ROYAL SOCIETY OF CHEMISTRY

www.rsc.org/advances

Journal Name

RSCPublishing

ARTICLE

Nanostructured $Bi_{(1-x)}Gd_{(x)}FeO_3$ – A Multiferroic Photocatalyst on its Sunlight Driven Photocatalytic Activity

Cite this: DOI: 10.1039/xoxxoooooox

Received ooth January 2012,
Accepted ooth January 2012

DOI: 10.1039/xoxxoooooox

www.rsc.org/

Sakar Mohan,[a] Balakumar Subramanian,[a,*] Indranil Bhaumik,[b] Pradeep Kumar Gupta,[b] and Sellamuthu N. Jaisankar,[c]

The photocatalytic activity of sol-gel synthesized nanostructured $Bi_{1-x}Gd_xFeO_3$ (x = 0, 0.05, 0.1, 0.15) particles on the degradation of methylene blue (MB) was demonstrated for the first time under sunlight. The X-ray diffraction (XRD) studies showed that the substitution induced structural changes in 10 and 15% Gd substituted BFO. The morphology analysis by field emission scanning (FESEM) and high resolution transmission electron microscopy (HRTEM) presented the composition driven particle size reduction and morphology changes in BFO from irregular to spherical shape. The band gap estimation by UV-visible diffuse reflectance spectroscopy revealed that increasing concentration of Gd significantly reduced the band gap of BFO from 2.38 eV to 2.29 eV. An anomalous magnetic enhancement was observed in $Bi_{0.90}Gd_{0.10}FeO_3$ nanoparticles due to the manifestation of antiferromagnetic (AFM) core — ferromagnetic (FM) shell-like structure that revealed by its *M-H* hysteresis curve. An increasing trend in the photocatalytic activity of BFO was observed with increasing concentration of Gd. In the case where an enhanced photocatalytic activity observed in $Bi_{0.85}Gd_{0.15}FeO_3$ could be due to its increased ferroelectric domains that drive the charge carriers to catalyst surface-dye interface leading to more effective degradation of the dye. Conversely, an anomalous photocatalytic activity was observed in $Bi_{0.90}Gd_{0.10}FeO_3$that should be attributed to its AFM/FM core/shell-like structure.

1. Introduction

Multiferroics refer to the multifunctional materials that exhibit simultaneous effects of ferroic properties such as ferroelectricity, ferromagnetism, ferroelasticity, etc. Perovskite bismuth ferrite ($BiFeO_3$–BFO) is one of the single-phase multiferroic materials that exhibits intrinsic spontaneous ferroelectricity (TC~1100 K) and G-type antiferromagnetism (TN~643 K) at room temperature.[1,2] BFO possesses rhombohedrally distorted structure and belongs to R3c space group.[3,4] Over the decades, extensive studies have been carried out on BFO to understand the science behind the features and functions of multiferroic materials. The ferroelectric property of BFO originates from the Bi-O hybridization due to the stereo-chemical activity of Bi $6s^2$ lone pair electrons and the magnetic property originates due to the partially filled 3d orbital of Fe^{3+} ions that leads to the manifestation of G-type antiferromagnetism (G-AFM).5, 6 In view of a unit cell of BFO crystal, the magnetic moments of Fe ions are coupled ferromagnetically within the pseudocubic (111) planes and coupled antiferromagnetically with respect to the adjacent planes.[7] Thereby, the established G-type AFM spin propagates through the crystal with an incommensurate long-wavelength period of 62 nm8 and cancels the macroscopic magnetization and limits the linear magneto-electric (ME) property in BFO.9 On the other hand, when the Fe magnetic moments are aligned perpendicular to the [111] axis, the crystal symmetry of BFO allows a "canted" AFM sublattice that results in a macroscopic magnetization known as weak ferromagnetism.[7,10]

However, the magnitude of spontaneous polarization and magnetization of bulk BFO is relatively low compared to the typical ferroelectric and ferromagnetic materials. Therefore, it is essential to improve both properties simultaneously to develop devices with enhanced multiferroic functionalities for versatile applications. Consequently, size-dependent magnetic properties have been obtained in nanoscale BFO particles.[11-13,18] Alternatively, controlling the dimensions of the material, such as thin film, fibrous, tubular, rod-like structures of pure and doped BFO are also found to exhibit dimension-dependent enhanced magnetic and ferroelectric properties.[14-17] Similarly, enhanced spontaneous ME and ferroelectric properties have been obtained in rare earth such as La, Nd, Sm, Tb, Gd-substituted BFO.[19-22] It was found that the incorporation of such

rare earth elements significantly changes the chemistry of BFO that drastically enhances its physical properties.

On the other hand, this multiferroic BFO is also recognized as a visible light-driven photocatalyst owing to its narrow band gap (~2.2 eV). Consequently, considerable amount of studies have been carried out on its visible light-driven photocatalytic ability to degrade various pollutants such as Congo red, Rhodamine B (RhB), methyl orange and methylene blue (MB).[23-25] Toward enhancing its photocatalytic ability on the degradation of pollutants, BFO has been synthesized by varying its structural parameters such as morphology,[23] size,[24] dimensions[25] and by varying its compositional parameters such as composites,[26] core/shell structuring,[27] substitution,[28] and Plasmon sensitizations.[29] However, sunlight-driven photocatalytic activities of BFO system are yet to be studied. To the best of our knowledge, there are hardly any report other than the one reported by us on sunlight-driven photocatalytic activity of BFO.[30] It is indeed fascinating to study the photocatalytic origin of BFO in the perspective of its perovskite structure and ferroelectric property. The distorted lattice system of perovskite-structured ferroelectrics possess significant impact on crystal fields that are capable of changing its electronic band structures and dipole–dipole interactions in the material that reflects in enhancing the production of photo-induced charge carriers (i.e. e^-/h^+ pairs) as well as the charge transfer and redox reactions at the surface of the photocatalyst.[31] Owing to such possibilities, the perovskite (ABO_3) structures offer smart ways of generating new materials for photocatalytic-based applications.[32] It is known that the intrinsic electric dipole moments of a ferroelectric material cause polarization alignment and result in the formation of ferroelectric domains.[33] While these ferroelectric domains interact with other phases (such as liquid, gas, metal surfaces, etc.), the overall surface reactivity of these ferroelectric material is significantly influenced and this changes its physical properties. Such changes mainly enhance their photo-reactivity by facilitating the production and separation of photo-induced electron-hole pairs in the materials.[34] It is very much possible for such phenomena to occur predominantly in the semiconducting ferroelectric material[35] as well as in multiferroic BFO as observed in this study.

Often, rigorous evaluation of materials and various phenomena associated with their properties under different experimental conditions are necessary to establish their versatility, and to understand the materials' property at their entirety. With this context, here we report the sunlight-driven photocatalytic activity of pure and Gd-substituted BFO on its ability to degrade the organic pollutant such as MB. The rare earth Gd was chosen as a substitution element because of its ionic radius 0.938Å, which is smaller than that of Bi^{3+} ions 1.17Å. Such replacement of smaller ionic radius element is expected to create a larger lattice distortion in BFO toward its chemical and physical property enhancements. Since Gd ions are magnetically active, the interaction between Bi^{3+} and Gd^{3+} may significantly enhance the magnetic property of BFO. Besides, enhancing the magnetic property of BFO is essential for its recovery and to separate it from the dye medium for further recycles or the safe disposal of the photocatalyst as can be viable in other iron oxide based systems.[36]

2. Experiment

2.1. Material synthesis

For the study, gadolinium-substituted BFO nanoparticles with substitution formula of $Bi_{(1-X)}Gd_{(X)}FeO_3$, where x = 0, 0.05, 0.1, 0.15, were prepared by the conventional sol-gel process. In a typical procedure, appropriate amount of bismuth (III) nitrate hydrate and iron (III) nitrate hydrate precursors were taken in the required stoichiometric ratio and dissolved in the de-ionized water. Citric acid with 1:1 stoichiometric ratio with respect to the metal nitrates was added to the above solution for gelation purposes. To this, 2 mL of nitric acid (70% conc.) was added and stirred for about 2 h to obtain a homogeneous sol. Further the sol was heated up to ~80^{o}C to obtain gel and dried to powder. Finally, the end-powders of all the compositions were annealed at 650^{o}C for 3 h to obtain the BFO phase.

2.2. Photocatalytic experiment

The organic dye MB was chosen for the photocatalytic studies. 1 mg MB was dissolved in 1 L of deionized water to prepare the solution of MB dye. Accordingly, $Bi_{1-x}Gd_xFeO_3$(x = 0, 0.05, 0.1, 0.15) catalyst was taken such that the amount of photocatalyst and dye was 50 mg and 1 mg respectively. Further, the mixture of dye and catalyst was kept under the irradiation of sun light. Subsequently, the degradation of MB was monitored by UV-visible absorption spectroscopy for every 1 h.

2.3. Materials and characterizations

The precursors were procured from Alfa Aesar (Puratronic, USA) with 99.99% purity. All the annealed samples were subjected to structural studies by X-ray diffraction (XRD) (PANalytical Instruments, Holland). Morphology studies by field emission scanning electron microscopy (FESEM) (Hitachi HighTech SU6600, Singapore) and high resolution scanning transmission electron microscopy (HRSTEM) (Techni G2 S-TWIN, FEI, The Netherlands) techniques. The magnetic study was carried out by vibrating sample magnetometer (VSM) (Lake Shore - 7404 VSM, USA). Finally, the optical and photocatalytic studies were carried out by UV-Visible diffuse reflectance/absorption spectroscopy (PerkinElmer, UV Lambda-600, USA), respectively.

3. Results and discussions

3.1. Crystal structure and phase analysis

The crystal structure and phase of $Bi_{1-x}Gd_xFeO_3$ (x = 0, 0.05, 0.1, 0.15) compositions were examined by XRD analysis and results are shown in Fig. 1(a). The diffraction pattern of pure BFO is well matched with the distorted rhombohedral

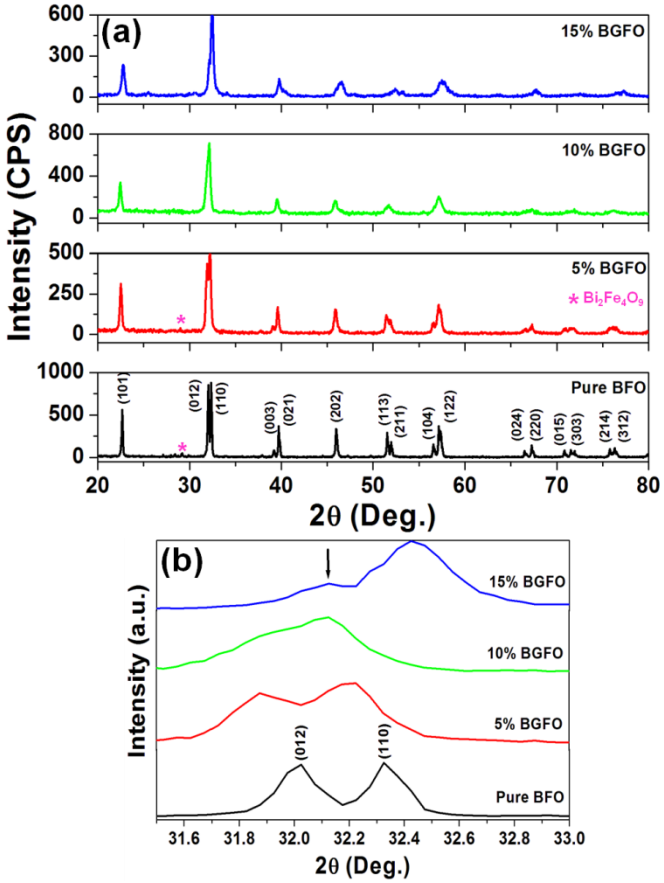

Fig. 1 XRD pattern of **(a)** $Bi_{1-x}Gd_xFeO_3$ (x=0, 0.05, 0.1, 0.15), **(b)** doublet peak (012) and (110) merging Gd-substituted BFO.

structure with R3c space group of $BiFeO_3$ system (JCPDS card No. 20-0169) and the observed peak merge and shift in the XRD pattern of Gd substituted compositions indicated the manifestation of structural changes in the host BFO due to Gd substitution. The existence of the typical non-perovskite $Bi_2Fe_4O_9$ secondary phase was observed in non-substituted BFO and $Bi_{0.95}Gd_{0.05}FeO_3$ composition with very small intensities.[37]

Table 1. Unit cell parameters of $Bi_{1-x}Gd_xFeO_3$ compositions

Composition	a = b (Å)	c (Å)	Cell volume (Å^3)
$BiFeO_3$	5.5839	13.8831	374.8769
$Bi_{0.95}Gd_{0.05}FeO_3$	5.5762	13.8530	373.0316
$Bi_{0.90}Gd_{0.10}FeO_3$	5.5657	13.7785	369.6263
$Bi_{0.85}Gd_{0.15}FeO_3$	5.5609	13.5002	361.5512

However, the higher concentration of Gd in BFO host prevented the formation of this secondary phase and the pure phase was obtained in $Bi_{0.90}Gd_{0.10}FeO_3$ and $Bi_{0.85}Gd_{0.15}FeO_3$ compositions. This proves that the substitution of a certain amount of Gd stabilizes the perovskite $BiFeO_3$ phase.[38] The crystallite size was calculated from the XRD pattern (maximum intensity peak) using Scherer's formula (t= 0.94λ/βcosθ) and found to be 68, 59, 53, and 42 nm for pure, 5, 10, and 15% Gd-substituted BFO, respectively. The calculated unit cell parameters such as lattice constants and cell volume of the compositions are shown in Table 1 and the graph plotted on the concentration of Gd Vs lattice constant and cell volume is shown in Fig. 1(c) and insert, respectively.

Further, it can be observed that the doublet peaks ((012) and (110)) of the BGFO compositions started merging with the increasing concentration of Gd in BFO and became as a single broadened peak for the $Bi_{0.90}Gd_{0.10}FeO_3$ composition as shown in Fig. 1(b). This could be due to its partial phase transformation from rhombohedral to orthorhombic phase ($Pn2_1a$) which allows polar ionic displacement in BFO along [010] direction.[39] Along with the merging of the doublet peak in $Bi_{0.85}Gd_{0.15}FeO_3$, an additional peak (indicated by an arrow mark) also appeared in its XRD pattern that could be due to the structural distortion from rhombohedral to pseudotetragonal structure.

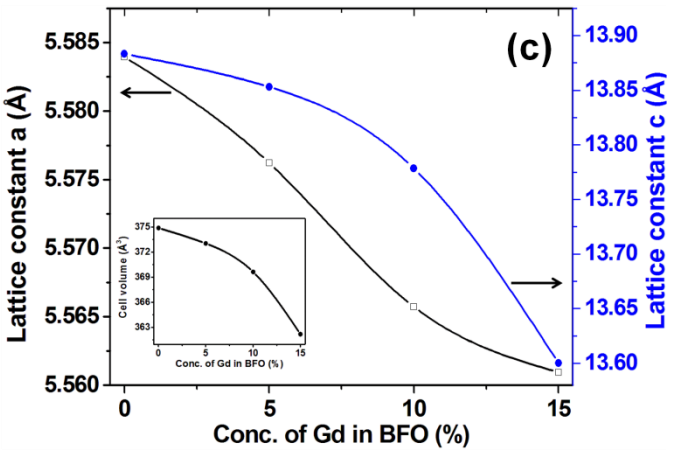

Fig. 1(c) Increasing concentration of Gd Vs lattice constant and cell volume (insert) of the compositions

This structural changes may further resulted in the splitting of $(100)_t$ and $(001)_t$ peaks that could be indexed to tetragonal symmetry.[40] These kinds of structural changes in BFO have already been reported, however, such structural changes in nanoscale BFO due to Gd substitution are different from those of La- or Nd-doped BFO ceramics and thin films, [37, 41, 42] and this may be essentially due to its smaller ionic radius and the distribution of Gd^{3+}ions in the nanoscale BFO host.

3.2. Morphology analysis

Figures 2 (a)–(d) show the FESEM images of pure and Gd-substituted BFO nanoparticles. The analysis showed that the average particle size of $Bi_{1-x}Gd_xFeO_3$ compositions decreases with increasing concentration of Gd from 5% to 15%. The reduction in the particle size was due to the inhabitation of the substituted Gd ions on the surface of the particles and this significantly suppressed the particle growth.[43] The morphology of pure BFO particles was found to be irregular and large in size ranging between 100 nm and 400 nm. Upon the increment of Gd concentration from 5 to 15%, the morphology of BFO started changing from its irregular to spherical shape and the particle size was also found to be reduced significantly. Particularly, a homogeneous size distribution of spherical

nanoparticles with an average size around 60 nm was obtained in $Bi_{0.85}Gd_{0.15}FeO_3$ composition.

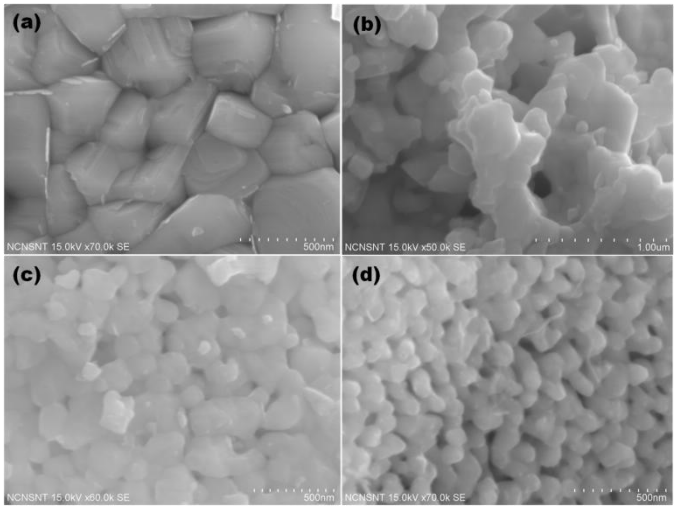

Fig. 2 FESEM images of **(a)** pure BFO, **(b)** $Bi_{0.95}Gd_{0.05}FeO_3$, **(c)** $Bi_{0.90}Gd_{0.10}FeO_3$, **(d)** $Bi_{0.85}Gd_{0.15}FeO_3$.

Figures 3(a)–(d) show HRTEM images of $Bi_{1-x}Gd_xFeO_3$ compositions and Figures 3 (e)–(f) show the lattice fringes of pure BFO and SAED pattern of all the compositions, respectively. It was also evident from these images that the particles were aggregated and possessed irregular and spherical shapes which is consistent with the FESEM images of the respective compositions. The observed size reduction with increasing Gd concentration was essentially attributed to the smaller ionic radius of Gd^{3+} ions compared to Bi^{3+} ions. As a consequence of this, the lattice contraction was also took place in the Gd substituted BFO, which can be corroborated with the calculated lattice parameters of the compositions given in the Table 1. Similarly, the reduced particle size of the compositions was clearly noticeable in the micrographs, especially in the case of $Bi_{0.85}Gd_{0.15}FeO_3$.

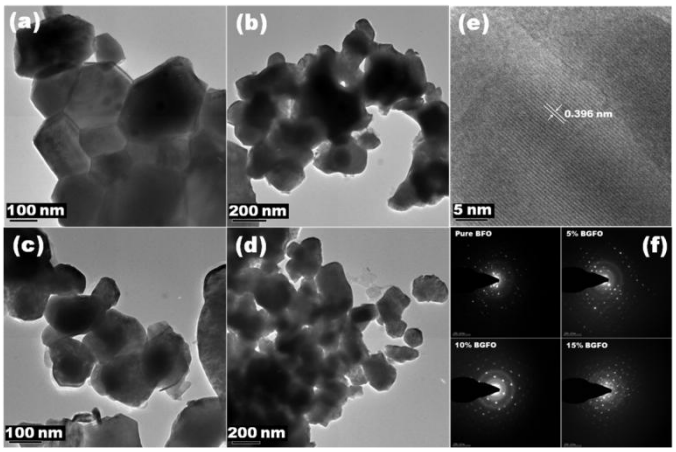

Fig. 3 HRTEM images of **(a)–(d)** $Bi_{1-x}Gd_xFeO_3$ (x=0, 0.05, 0.1, 0.15), respectively, **(e)** fringes of pure BFO, **(f)** SAED of $Bi_{1-x}Gd_xFeO_3$ compositions.

The observed lattice fringes of pure BFO essentially revealed that the BFO phase formation occurred with a high order of crystalline nature. The rhombohedral structure of BFO was also confirmed from the measured lattice distance of 0.396 nm along (012) plane in the HRTEM images as shown in Fig.3(e) and the value was consistent with the reported lattice distance value of rhombohedral-structured pure $BiFeO_3$ systems.[12, 44]

The distorted SAED patterns of pure and 5% BGFO compositions as shown in Fig. 3(f) suggested that the defective nature and the mixed phase of the material ($BiFeO_3$ and $Bi_2Fe_4O_9$ phases). A sharp and distinct circular ring SAED pattern of $Bi_{0.90}Gd_{0.10}FeO_3$ composition revealed the manifestation of high order of crystallinity in the particles and the discrete spots suggested the presence of defect-free polycrystalline nature and systemic lattice orientation in the nanoparticles. The observed complex SAED pattern of $Bi_{0.85}Gd_{0.15}FeO_3$ composition may be due to its structural transformation from rhombohedral to pseudotetragonal like structure.

3.3. Magnetization studies

The room temperature magnetic behavior (*M–H* curves) of $Bi_{1-x}Gd_xFeO_3$ compositions are shown in Fig. 4(a).

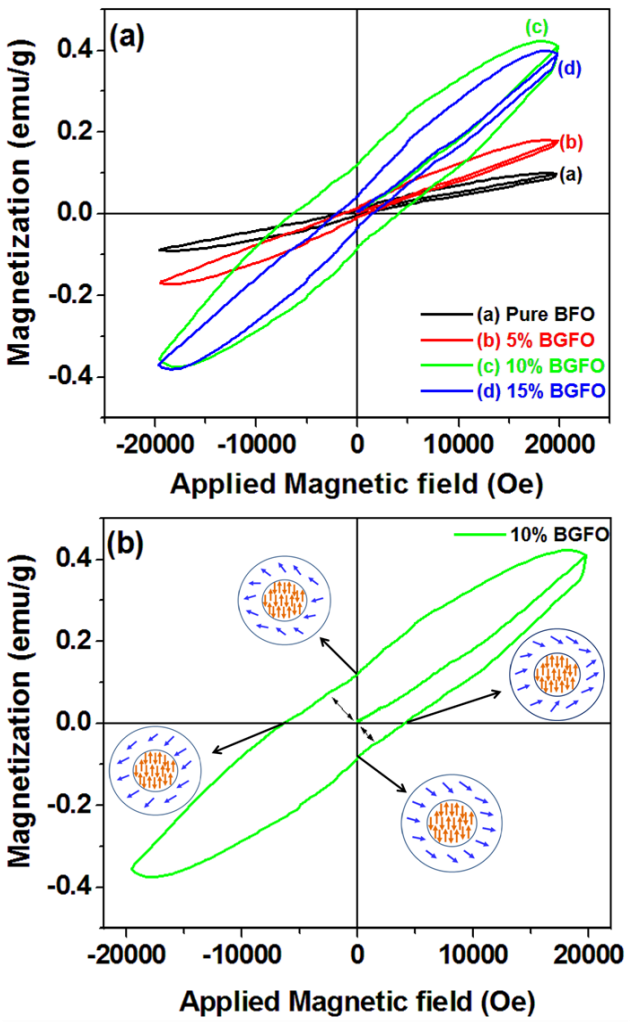

Fig. 4 (a) Magnetization of *M–H* curves of $Bi_{1-x}Gd_xFeO_3$ compositions, **(b)** *M–H* curve of $Bi_{0.90}Gd_{0.10}FeO_3$that reflects the manifestation of AFM/FM core/shell structure.

It was evident from the *M–H* hysteresis curves that increment of Gd ions in BFO host increases its magnetic properties. However, an enhanced magnetic property was observed in $Bi_{0.90}Gd_{0.10}FeO_3$ compared to other Gd-substituted BFO compositions. This could be due to the following factors: Firstly, it may be due to the partial change of crystal phase from its parent rhombohedral to orthorhombic phase. As a result of this, it is possible for $Bi_{0.90}Gd_{0.10}FeO_3$ lattices to have a larger distribution of iron (Fe) ions with valence (+3) states in the [FeO_6] clusters that cause an imbalanced state between the anti-parallel sub-lattices of Fe^{3+} ions with appropriate electron densities[45] and induce the FM orientation at the surface of the nanoparticles owing to its larger surface area. Consequently, this variation in the electron density across the volume to the surface might have led to the formation of AFM core and FM surface (core/shell) structure in $Bi_{0.90}Gd_{0.10}FeO_3$ nanoparticles.[46,47] Accordingly, the manifestation of such AFM/FM - core/shell structure in this particular composition was evident from the observed displacement of *M–H* hysteresis curve toward negative and positive axis as shown in Fig. 4(b). Secondly, it is well known that Gd ions are magnetically active with S = 7/2 spins that also may have significantly contributed to the FM coupling between Gd^{3+} and Fe^{3+} ions in this particular composition as a result of this partial phase change from rhombohedral to orthorhombic as dictated by its XRD pattern.[48]

3.4. Band gap estimation

The band gap of the synthesized $Bi_{1-x}Gd_xFeO_3$ compositions was estimated from the obtained UV-Visible diffuse reflectance spectra as shown in Fig. 5(a) and the estimated band gap values are 2.38, 2.36, 2.32, 2.29eV for $Bi_{1-x}Gd_xFeO_3$ where x = 0, 0.05, 0.1 and 0.15 respectively.

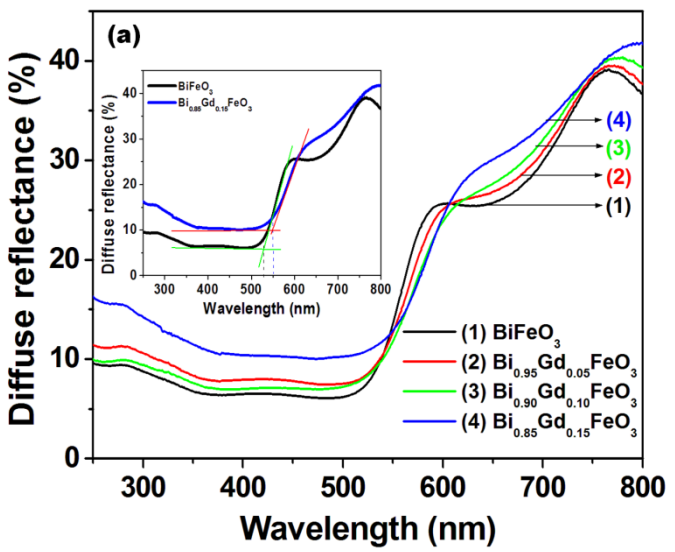

Fig. 5 (a) UV-DRS spectra of $Bi_{1-x}Gd_xFeO_3$ compositions

It was found that band gap of BFO decreases with increasing concentration of Gd in BFO host. Despite the decrease in particle size with increasing Gd concentration, the observed reduction in band gap may be due to charge transfer from the electron donor levels formed by the 4f orbital of Gd^{3+} ions to the conduction band of the host BFO[49a,b] as schematically represented in Fig. 5(b).

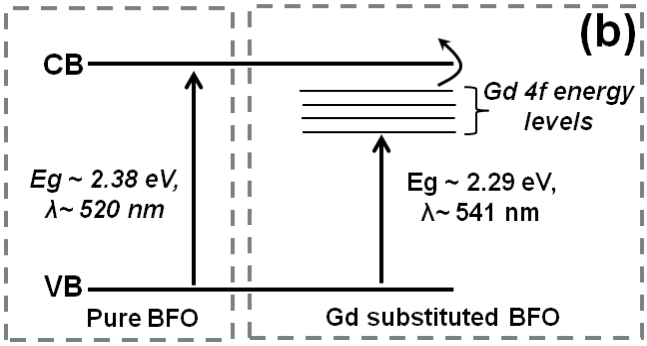

Fig. 5 (b). The concept of band gap engineering in Gd-substituted BFO.

It is known that the band gap of BFO is formed by the orbital overlap between the oxygen *2p* and iron *3d* levels.[49c] In Gd-substituted BFO, the Gd *4f* level lies below the conduction band of host BFO as shown in Fig. 5(b). This newly formed Gd *4f* energy level effectively interacts with valence O *2p* orbital and leads to the charge-transfer transition from Gd energy levels to the conduction band of BFO and therefore the band gap was found to be reduced in Gd-substituted BFO compared to the pure.

3.5. Photocatalytic studies

As described in Section 2.2, the appropriate amount of dye and $Bi_{1-x}Gd_xFeO_3$ (x = 0, 0.05, 0.1, 0.15) photocatalyst mixture solution was taken and exposed to the sunlight to study their photocatalytic efficiency on the degradation of MB. The individual degradation spectra of MB by $Bi_{1-x}Gd_xFeO_3$ nanoparticles and their C/C_0 ratio are shown in the Fig. 6(a)–(e). At end of 4 h of sunlight exposure, the $Bi_{1-x}Gd_xFeO_3$ (x = 0, 0.05, 0.1, 0.15) were degraded by 58%, 72%, 94%, and 92% of the dye, respectively. As shown in the C/C_0 graph, the photocatalytic activity of BFO increased with increasing concentration of Gd. However, $Bi_{0.90}Gd_{0.10}FeO_3$ showed an anomalous enhancement in degradation of up to 94% compared to other compositions. This can be understood by considering the perspective of the observed anomalous improvement in weak FM nature of $Bi_{0.90}Gd_{0.10}FeO_3$ composition.

3.5.1. Photocatalytic mechanism in $Bi_{1-x}Gd_xFeO_3$ nanoparticles

It is discussed in the sections 3.1 and 3.2 that the orthorhombic phase of $Bi_{0.90}Gd_{0.10}FeO_3$ allows polar displacements in BFO and the increased electron density at the surface of $Bi_{0.90}Gd_{0.10}FeO_3$ enhanced its magnetic property by forming the AFM-core/FM-surface. It is therefore during the photocatalytic process, this electron density which is an electron cloud in the FM surface might have facilitated the photocatalytic enhancement in the following two ways. Firstly, it is possible for these electron clouds behaved like a large local electric field (likely a polarized surface) and lead BFO to

strongly absorb the photons and facilitate the generation of more number of electron-hole pairs in the photocatalyst. Secondly, the recombination rate of these electron-hole pairs can also be significantly reduced by trapping them in these electron clouds. As a result, these trapped carriers can effortlessly promote to the photocatalyst–dye interface and significantly degrade the dye as depicted in Fig. 7 (a)-(c).

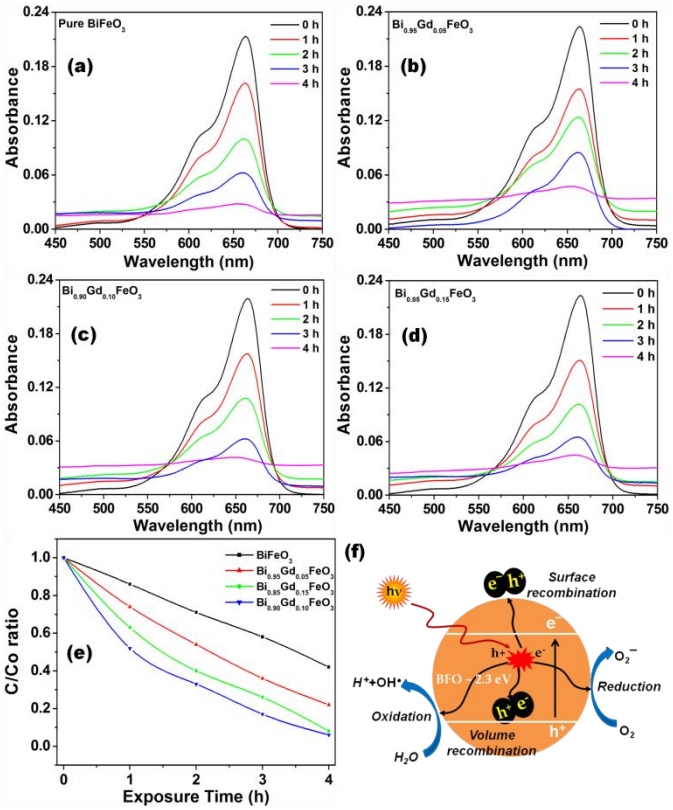

Fig. 6 Degradation graph of **(a)–(d)** $Bi_{1-x}Gd_xFeO_3$ (x = 0, 0.05, 0.1, 0.15) compositions, **(e)** C/C_0 ratio of the compositions, **(f)** photocatalytic mechanism in BFO.

Further, the significant improvement in the photocatalytic activity of 5% and 15% Gd-substituted BFO compared to pure can be explained as follows. It is known that whenever a semiconductor material establishes a contact with other phases (such as gas, liquids, metal surfaces, etc.), it is possible for the formation of a space charge double layer along with the redistribution of electric charges at their interfaces.[39a, 50] Similarly in BFO, which is a semiconducting ferroelectric material, the dipole-dipole interactions cause polarization and produce ferroelectric (negative and positive polarization) domains.

These ferroelectric domains can be significantly influenced by the interactions with other phases and results the polarization-charge imbalanced surfaces.[34,51] Such charge imbalance may be balanced by the mobile carriers of the host materials and/or through the adsorption of other phases on the host surface. During such charge balancing process, the energy band of the host materials bend downwards or upwards at near-surface regions and forms accumulation and depletion layers as shown in Fig. 8(a)-(b). The upward and downward band bending occurs when the effective surface charge becomes more negative and positive, respectively.[50,52]

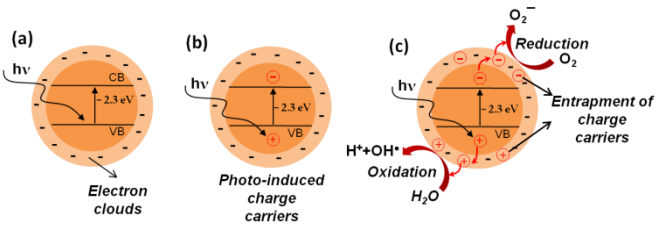

Fig. 7 (a) AFM/FM core/shell structure of $Bi_{0.90}Gd_{0.10}FeO_3$ nanoparticles, **(b)** development of photo-induced charge carriers in the particle, **(c)** entrapment of charge carriers in the surface electron clouds of the particle that facilitates the photocatalytic activity.

In such circumstances, with the irradiation of light, the formation of electron-hole pairs and their separation get enhanced in the catalyst. Eventually, these photo-induced charge carriers perform reduction and oxidation reactions on the surface of positive and negative domains, respectively. Therefore, it is evident that the enhancement in the ferroelectric property of a semiconducting ferroelectric material may directly enhance its photocatalytic activity as well.

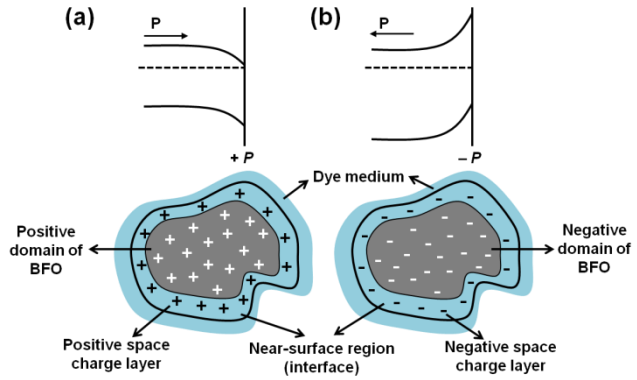

Fig. 8 Formation of space charge interface layer around **(a)** positive domain, **(b)** negative domain of the ferroelectric $Bi_{1-x}Gd_xFeO_3$ and causing band bending.

Accordingly, the observed enhanced photocatalytic efficiency of $Bi_{0.85}Gd_{0.15}FeO_3$ composition may be due to its enhanced ferroelectric property through the formation of more number of ferroelectric polarization domains. This could be substantiated from the XRD pattern of $Bi_{0.85}Gd_{0.15}FeO_3$ which suggests that the structural distortion of BFO from rhombohedral to pseudotetragonal like structure may enhance its ferroelectric polarization. Moreover, such structural distortion enhances the ferroelectric property of BFO as claimed in this study can also be found in the literature.[43,53-54] Such perspectives of investigating BFO as a semiconducting ferroelectric material may lead to better understanding of its photocatalytic origin as an attempt made in this study.

4. Conclusions

In summary, nanoparticles of $Bi_{1-x}Gd_xFeO_3$ (x = 0, 0.05, 0.1, 0.15) were synthesized by sol-gel method and their sunlight driven photocatalytic efficiency on the degradation of MB under the sunlight was studied for the first time. XRD analysis

revealed that the substitution of Gd at 10% and 15% changed the crystal structure of BFO from rhombohedral to orthorhombic and pseudotetragonal like structure respectively. The band gap of $Bi_{1-x}Gd_xFeO_3$ compositions was decreasing with increasing concentration of Gd that suggested the formation of electron donor levels by 4*f* orbital of Gd^{3+} ions to the conduction band of BFO. Further, the magnetic property of BFO also improved with Gd substitution. The observed anomalous magnetic property of $Bi_{0.90}Gd_{0.10}FeO_3$ could be due to the formation of AFM-FM core/shell-like structure that was revealed by its *M-H* hysteresis curve. The enhanced photocatalytic efficiency of $Bi_{1-x}Gd_xFeO_3$ compositions can be attributed to its surface charge modification that occurred by the charge interaction at the interface of BFO-dye medium. The improved photocatalytic efficiency of $Bi_{0.85}Gd_{0.15}FeO_3$ nanoparticles could be due to the interaction between the ferroelectric domains and dye medium through the formation of space charge layers where the charge transfer and redox reactions get enhanced and led to the degradation of the dye very effectively. On the other hand, the anomalous photocatalytic enhancement of $Bi_{0.90}Gd_{0.10}FeO_3$ nanoparticles could be attributed to its enhanced surface reactivity due to the formation of AFM/FM core/shell structure in which the photo-induced carriers were effectively trapped by the electron clouds of FM surface and significantly reduced the charge carrier recombination and increased the redox reactions. It was evident from the study that the exploration of the photocatalytic origin of BFO in terms of its semiconducting ferroelectric property would give new insights to develop efficient photocatalysts for solar-based photocatalytic applications.

Acknowledgement

Authors gratefully acknowledge the Council of Scientific and Industrial Research (CSIR), Govt. of India for funding to carry out this research project.

Notes and references

[a,*] National Centre for Nanoscience and Nanotechnology, University of Madras, Guindy campus, Chennai 600025, India. Fax: 044-22352494/22353309; Tel: 044-22202749, E-mail: balasuga@yahoo.com
[b] Raja Ramanna Centre for Advanced Technology, Indore 452013, India
[c] Polymer Lab, Central Leather Research Institute, Chennai 600020, India

1. S. V. Kiselev, R. P. Ozerov, G. S. Zhdanov, *Sov. Phys. Dokl.*, 1963, **7**, 742.
2. J. R. Teague, R. Gerson, W. J. James, *Solid State Commun.*, 1970, **8**, 1073.
3. C. Michel, J. M. Moreau, G. D. Achenbach, R. Gerson, W. J. James, *Solid State Commun*., 1969, **7**, 701.
4. F. Kubel, H. Schmid, *Acta. Crystallogr. Sect. B. Struct. Sci*., 1990, **46**, 698.
5. Z. X. Cheng, A. H. Li, X. L. Wang, S. X. Dou, K. Ozawa, H. Kimura, S. J. Zhang, T. R. Shrout, *Journal of Applied Physics*, 2008, **103**, 07E507.
6. I. Sosnowska, T. Peterlin-Neumaier, E. Steichele, *Journal of Physics C*, 1982, **15**, 4835.
7. I. E. Dzyaloshinskii, *Sov. Phys. JETP*., 1957, **5**, 1259.
8. Y. H. Lee, J. M. Wu, C. H. Lai, *Appl. Phys. Lett*., 2006, **88**, 042903.
9. Y. F. Popov, A. K. Zvezdin, G. P. Vorobev, A. M. Kadomtseva, V. A. Murashev, D. N. Rakov, *JETP Lett*., 1993, **57**, 69.
10. T. Moriya, *Phys. Rev*., 1960, **120**, 91.
11. F. Gao, Y. Yuan, K. F. Wang, X. Y. Chen, F. Chen, J. M. Liu, Z. F. Ren, *Appl. Phys. Lett.*, 2006, **89**, 102506.
12. Y. Du, Z. X. Cheng, S. X. Dou, D. J. Attard, X. L. Wang, *J. Appl. Phys.*, 2011, **109**, 073903.
13. R. Mazumder, P. S. Devi, D. Bhattacharya, P. Choudhury, A. Sen, M. Raja, *Appl, Phys. Lett.*, 2007, **91**, 062510.
14. D. Lee, M. G. Kim, S. Ryu, H. M. Jang, S. G. Lee, *Appl. Phys. Lett.*, 2005, **86**, 222903.
15. C. Ederer, N. A. Spaldin, *Phys. Rev. B.*, 2005, **71**, 060401.
16. Z. X. Cheng, X. L. Wang, S. X. Dou, H. Kimura, K. Ozawa, *Phys. Rev. B.*, 2008, **77**, 092101.
17. J. B. Neaton, C. Ederer, U. V. Waghmare, N. A. Spaldin, K. M. Rabe, *Phys. Rev. B.*, 2005, **71**, 014113.
18. L. Fang, J. Liu, S. Ju, F. Zheng, W. Dong, M. Shen, *Appl. Phys. Lett.*, 2010, **97**, 242501.
19. Y. Yao, W. Liu, Y. Chan, C. Leung, C. Mak, *Int. J. Appl. Ceram. Technol.*, 2011, **8**, 1246.
20. X. Yan, J. Chen, Y. Qi, J. Cheng, Z. Meng, *J. Eur. Ceram. Soc*., 2010, **30**, 265.
21. G. L. Bras, D. Colson, A. Forget, N. Genand-Riondet, R. Tourbot, P. Bonville, *Phys. Rev. B.*, 2009, **80**, 134417.
22. R. Rai, S. K. Mishra, N. K. Singh, S. Sharma, A. L. Kholkin, *Curr. Appl. Phys*., 2011, **11**, 508.
23. Li Shun, Lin Yuan-Hua, Bo-Ping Zhang, Yao Wang, Ce-Wen Nan, *J. Phys. Chem. C*., 2010, **114**, 2903.
24. Feng Gao, Xinyi Chen, Kuibo Yin, Shuai Dong, Zhifeng Ren, Fang Yuan, Tao Yu, Zhigang Zou, Jun-Ming Liu, *Adv. Mater*., 2007, **19**, 2889.
25. Wei Wang, Nan Li, Yue Chi, Yanjuan Li, Wenfu Yan, Xiao tian Li, Changlu Shao, *Ceramics International.*, 2013, **39**, 3511.
26. M. Sakar, S. Balakumar, P. Saravanan, S. N. Jaisankar, *AIP Conf. Proc.*, 2013, **1512**, 228.
27. Yi Liu, Ruzhong Zuo, Shishun Qi, *Journal of Molecular Catalysis A: Chemical*, 2013, **376**, 1.
28. Yan-Nan Feng, Huan-Chun Wang, Yi-Dong Luo, Yang Shen, Yuan-Hua Lin, *J. Appl. Phys.*, 2013, **113**, 146101.
29. Shun Li, Jianming Zhang, Md Golam Kibria, Zetian Mi, Mohamed Chaker, Dongling Ma, Riad Nechache, Federico Rosei, *Chem. Commun.*, 2013, **49**, 5856.
30. M. Sakar, S. Balakumar, *RSC Adv.*, 2013, **3**, 23737.
31. (a) X. B. Chen, S. H. Shen, L. J. Guo, S. S. Mao, *Chemical Reviews*., 2010, **110**, 6503. (b) K. Maeda, *Journal of Photo- chemistry and Photobiology C*, 2011, **12**, 237.
32. (a) C. H. Li, K. C. K. Soh, P. Wu, *Journal of Alloys and Compounds*, 2004, **372**, 40. (b) D. F. Wang, J. H. Ye, T. Kako, T. Kimura, *Journal of Physical Chemistry B*, 2006, **110**, 15824. (c) D. F. Wang, T. Kako, J. H. Ye, *Journal of the American Chemical Society*, 2008, **130**, 2724.
33. V. M. Fridkin, Ferroelectric Semiconductors. Consultants Bureau: New York, 1980.
34. S. V. Kalinin, D. A. Bonnell, T. Alvarez, X. Lei, Z. Hu, J. H. Ferris, *Nano Lett*., 2002, **2**, 589.
35. A. M. Schultz, Y. Zhang, P. A. Salvador, G. S. Rohrer, *ACS Appl. Mater. Interfaces*, 2011, **3**, 1562.
36. (a) J. S. Chen, C. P. Chen, J. Liu, R. Xu, S. Z. Qiao, X. W. Lou, *Chemical Communications*, 2011, **47**, 2631, (b) Y. Liu, L. Yu, Y. Hu, C. F. Guo, F. M. Zhang, X. W. Lou, *Nanoscale,2012*, **4**, 183.
37. (a) Y. H. Lin, Q. Jiang, Y. Wang, C. W. Nan, *Appl. Phys. Lett*., 2007, **90**, 172507. (b) V. B. Naik, R. Mahendiran, *Solid State Commun*., 2009, **149**, 754.
38. C. Fanggao, S. Guilin, F. Kun, Q. Ping, Z. Qijun, *J. Rare Earth*, 2006, **24**, 273.
39. (a) R. Guo, L. Fang, W. Dong, F. Zheng, M. Shen, *J. Phys. Chem. C*., 2010, **144**, 21390. (b) V. A. Khomchenko, V. V. Shvartsman, P. Borisov, W. Kleemann, D.A. Kiselev, I. K. Bdikin, J. Vieira, L. MA Kholkin, *Acta Mater*, 2009, **57**, 5137.
40. G. L. Yuan, S. W. Or, J. M. Liu, Z. G. Liu, *Appl. Phys. Lett*., 2006, **89**, 052905.
41. H. Uchida, R. Ueno, H. Funakubo, S. Koda, *J. Appl. Phys.*, 2006, **100**, 014106.
42. S. T. Zhang, L. H. Pang, Y. Zhang, M. H. Lu, Y. F. Chen, *J. Appl. Phys.*, 2006, **100**, 114108.

43. Gurmeet Singh Lotey, N. K. Verma, *J. Nanopart. Res.*, 2012, **14**, 742.
44. S. K. Pradhan, J. Das, P. P. Rout, S. K. Das, *Journal of Magnetism and Magnetic Materials*, 2010, **322**, 3614.
45. T. J. Park, G. C. Papaefthymiou, A. J. Viescas, A. R. Moodenbaugh, S. S. Wong, *Nano Lett*., 2007, **7**, 766.
46. (a) S. R. Das, R. N. P. Choudhary, P. Bhattacharya, R. S. Katiyar, P. Dutta, A. Manivannan, M. S. Seehra, *J. Appl. Phys*., 2007, **101**, 034104. (b) M. Sakar, S. Balakumar, P. Saravanan, S. N. Jaisankar, *Mat. Res. Bul.*, 2013, **48**, 2878.
47. G. D. Hu, S. H. Fan, C. H. Yang, W. B. Wu, *Appl. Phys. Lett.*, 2008, **92**, 192905.
48. Rajasree Das, Tanushree Sarkar, K. Mandal, *J. Phys. D. Appl. Phys.*, 2012, **45**, 455002.
49. (a) Tinghong Hou, Jian Mao, Haibing Pan, Mingjing Tu, *Journal of Nanoparticle Research*, 2006, **8**, 293. (b) Z. Li, H. Xue, X. Wang, X. Fu, *J. Molec. Catal. A: Chem*, 2006, **260**, 56. (c) Gustau Catalan, James F. Scott, *Adv. Mater*., 2009, **21**, 2463.
50. L. Amy, Linsebigler Guangquan Lu, T. John, Jr. Yates, *Chem. Rev.*, 1995, **95**, 735.
51. (a) Feng Yan, Guannan Chen, Li Lu, Jonathan E. Spanier, *ACS Nano*., 2012, **6**, 2353. (b) J. L. Giocondi, G. S. Rohrer, *Chem. Mater*., 2001, **13**, 241.
52. (a) Yiling Zhang, Andrew M. Schultz, Paul A. Salvador, Gregory S. Rohrer, *J. Mater. Chem.*, 2011, **21**, 4168. (b) J. L. Giocondi, G. S. Rohrer, *J. Phys. Chem*., 2001, **B 105**, 8275.
53. D. Kan, L. Palova, V. Anbusathaiah, C. J. Ching, S. Fujino, V. Nagarajan, K. M. Rabe, I. Takeuchi, *Adv. Funct. Mater.*, 2010, **20**, 1108.
54. D. P. Dutta, B. P. Mandal, Ratna Naik, Gavin Lawes, A. K. Tyagi, *J. Phys. Chem. C*., 2013, **117**, 2382.

Graphical abstract

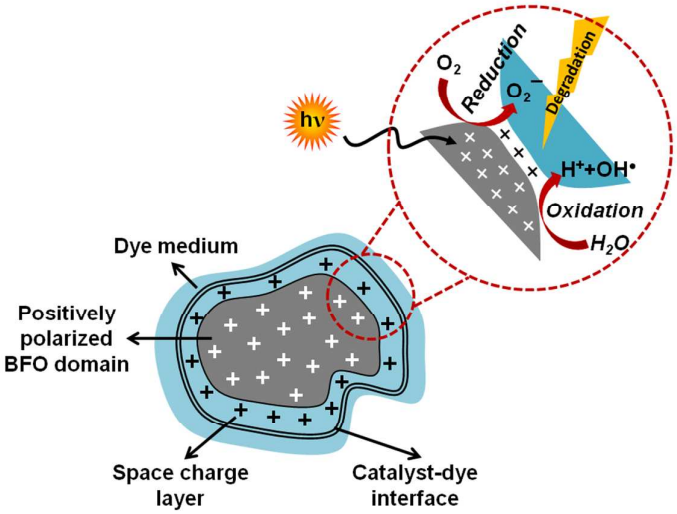

Novelty of the work

We report the manifestation of sunlight driven photocatalytic activity in the nanostructured Gd substituted bismuth ferrite ($BiFeO_3$) multiferroic photocatalyst.